Structural and magnetic properties of $Al_2O_3/Ni_{81}Fe_{19}$ thin films: from superparamagnetic nanoparticles to ferromagnetic multilayers

2005 J. Phys.: Condens. Matter 17 5027

(http://iopscience.iop.org/0953-8984/17/33/007)

INSTITUTE OF PHYSICS PUBLISHING JOURNAL OF PHYSICS: CONDENSED MATTER

J. Phys.: Condens. Matter **17** (2005) 5027–5036 doi:10.1088/0953-8984/17/33/007

Structural and magnetic properties of $Al_2O_3/Ni_{81}Fe_{19}$ thin films: from superparamagnetic nanoparticles to ferromagnetic multilayers

I L Soroka[1], V Stanciu[2], J Lu[2], P Nordblad[2] and B Hjörvarsson[1]

[1] Department of Physics, Uppsala University, Box 530, SE-751 21 Uppsala, Sweden
[2] Department of Engineering Science, Uppsala University, Box 534, SE-751 21 Uppsala, Sweden

E-mail: Inna.Soroka@fysik.uu.se

Received 1 April 2005
Published 5 August 2005
Online at stacks.iop.org/JPhysCM/17/5027

Abstract

$Al_2O_3/Ni_{81}Fe_{19}$ multilayer films were produced by sequential magnetron sputter deposition on thermally oxidized Si(001) substrates. It was shown that by varying the thickness of the $Ni_{81}Fe_{19}$ layer from 8 to 30 Å, while keeping the other parameters unchanged, one can control the film structure from nanoclusters to continuous multilayers. The nanoclustered sample is superparamagnetic while the continuous samples show ferromagnetic behaviour. The magnetic moments per atom of the $Ni_{81}Fe_{19}$ layers decrease with decreasing amount of metallic deposits, indicating the presence of nonmagnetic layers at the interfaces. The thicknesses of these layers are determined to be about 1 Å for the flat continuous film and 3.8 Å for the nanoclustered film. The existence of nonmagnetic layers may be interpreted in terms of the formation of antiferromagnetic oxides at the interfaces.

1. Introduction

Magnetic, optical, mechanical and transport properties of metal–insulator films are strongly dependent on their microstructure. One of the most important aspects in this context is the interface quality, i.e. roughness, thickness variation and the chemical uniformity. For example, the transport properties of magnetic tunnel junctions (MTJ) [1] are strongly affected by the quality of the insulating barrier and ferromagnetic/insulator interfaces [2–4]. The spin polarization of the tunnelling current of permalloy has been enhanced from 32% to 57% by improving the quality of the alumina barrier and the metal/alumina interfaces [5]. The results presented by Bowen *et al* [6] show the possibility of achieving a large amplitude of tunnelling magnetic resistance (TMR), up to 60%, provided that the MTJ have very sharp and well defined interfaces. Thus, studies of MTJ are now focused on the fabrication of junctions with high interface quality. Sputtering is widely used for producing such films [7].

Substrate temperature, gas pressure, oxidation time as well as the thickness of the layers influence the quality of metal–insulating structures. A substantial amount of work has therefore been devoted to investigating the effect of these factors on the resulting multilayer quality [8–12]. In particular, the thickness variations of the metallic layers are found to play an important role for the structural morphology of ferromagnetic/insulator films. In [13] it was shown that well defined Co/MgO layer structures are formed when the Co layers are thicker than 16 Å. The Co layers become discontinuous when their thicknesses are 12 Å or thinner. Moreover, in this thickness range the magnetic properties are substantially influenced by the interfaces: the sample with discontinuous Co layers is superparamagnetic at room temperature, while the continuous layers exhibit ferromagnetic behaviour.

The magnetism of thin films can be decreased by the interaction of a deposited metal with oxide substrates. It was found that the metal atoms can establish chemical bonds directly with the oxygen anions at the Al_2O_3 [14]. Therefore, the existence of thin antiferromagnetic FeO [15] and NiO [16] regions at the interfaces has to be considered when studying the $Ni_{81}Fe_{19}$/alumina multilayers.

In the present work we explore the interfacial quality and corresponding magnetic properties of the $Al_2O_3/Ni_{81}Fe_{19}$ multilayer films (grown on thermally oxidized Si(001) substrates) with different nominal thickness of the $Ni_{81}Fe_{19}$ layer, by means of x-ray reflectometry (XRR), transmission electron microscopy (TEM), superconducting quantum interference device (SQUID) magnetometry and magneto-optical Kerr effect (MOKE) measurements.

2. Experimental procedure

The $Al_2O_3/Ni_{81}Fe_{19}$ multilayer films were grown in an ultrahigh vacuum chamber by sequential magnetron sputter deposition on thermally oxidized SiO_2/Si substrates. Sputtering was carried out in an Ar (99.999%) atmosphere of 2.5 mTorr at ambient temperature, with rf and dc power inputs of 40 and 60 W for Al_2O_3 (99.99%) and $Ni_{81}Fe_{19}$ (99.99%) targets, respectively. The resulting deposition rates were 0.04 Å s^{-1} for Al_2O_3 and 0.48 Å s^{-1} for $Ni_{81}Fe_{19}$. The thickness of the Al_2O_3 layers was kept constant, equal to 18 Å for all the films. The quoted $Ni_{81}Fe_{19}$ layer thickness refers to the nominal thickness t_n (i.e. the thickness that would occur if the deposits were flat and homogeneous) to characterize the amount of the deposited metal. Thus, the nominal thickness of the $Ni_{81}Fe_{19}$ layer was varied from 8 to 30 Å. All samples contained ten repeats of one bilayer.

The structural quality of the films was determined by means of x-ray reflectivity measurements using a Siemens D5000 diffractometer (Cu Kα, $\lambda = 1.54$ Å) and cross-sectional TEM using Philips Tecnai F30ST operated at 300 kV with a point resolution of 2.05 Å. The magnetic properties were investigated by using a magneto-optical Kerr effect (MOKE) set-up at room temperature in a longitudinal geometry and a Quantum Design MPMSXL SQUID magnetometer.

3. Results and discussion

3.1. Structural characterization

The influence of the nominal thickness of the $Ni_{81}Fe_{19}$ layer on the microstructure is illustrated in figures 1 and 2.

In figure 1 a TEM image for the sample with 30 Å thick $Ni_{81}Fe_{19}$ layers is shown. The TEM micrograph clearly shows well defined interfaces and small thickness variation of the

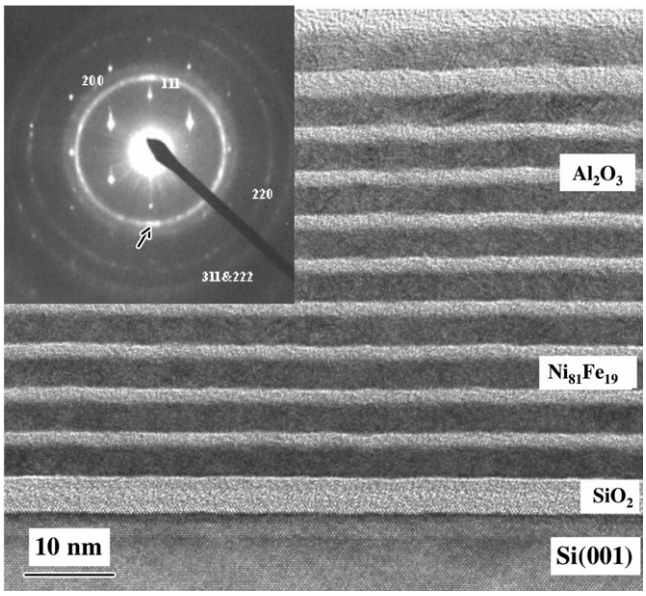

Figure 1. Cross-section transmission electron micrograph for $[Al_2O_3(18\ Å)/Ni_{81}Fe_{19}(30\ Å)]_{10}$ multilayer film. The diffraction spots in the inset are from the Si substrate. The arrow in the SAED pattern points out a textured diffraction ring from the (111) plane.

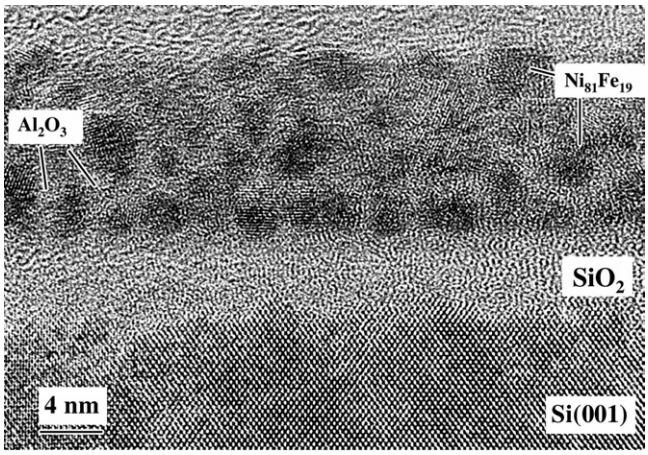

Figure 2. Cross-section transmission electron micrograph of $Ni_{81}Fe_{19}$ nanoclusters in Al_2O_3 matrix.

layers. Moreover, convergent beam electron diffraction analysis reveals that the $Ni_{81}Fe_{19}$ (black) layers are polycrystalline, while the Al_2O_3 (white) layers are amorphous. The selected area electron diffraction (SAED) pattern (inset in figure 1) corresponds to an FCC crystal structure of $Ni_{81}Fe_{19}$, with a cell parameter of 3.54 ± 0.03 Å, which is identical to the lattice constant of bulk $Ni_{81}Fe_{19}$ random alloy [17]. The labelled diffraction rings in the SAED pattern indicate the interatomic planes in the FCC structure; a slight (111) texture of the $Ni_{81}Fe_{19}$ layer is evident.

A micrograph of the sample with the thinnest ($t_n = 8$ Å) $Ni_{81}Fe_{19}$ layers is shown in figure 2. As seen in the figure, the $Ni_{81}Fe_{19}$ layers are discontinuous and, apparently, consisting of monocrystalline nanoparticles embedded in an amorphous Al_2O_3 matrix. The histogram of the particle size distribution (figure 3) obtained from the TEM image can be fitted with a

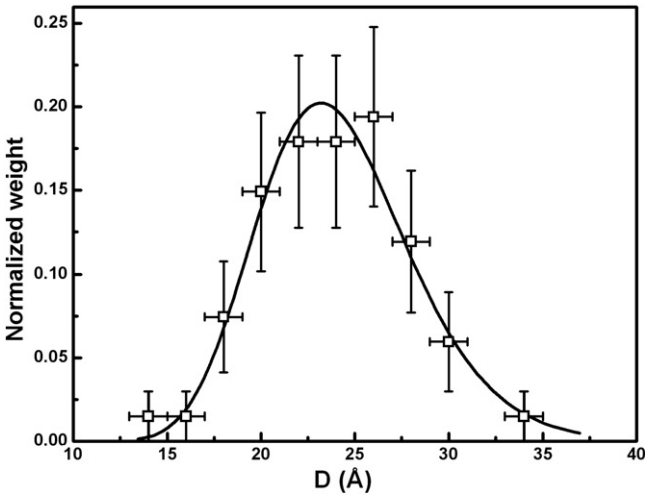

Figure 3. Histogram of the $Ni_{81}Fe_{19}$ particle diameters, as observed in TEM images (symbols). The line is a fit to a log-normal distribution with $D_0 = 24$ Å and $\sigma_D = 0.17$.

log-normal distribution function [18, 19]:

$$p(D) = \frac{1}{D\sigma_D\sqrt{2\pi}} \exp\left(\frac{-\ln^2 \frac{D}{D_0}}{2\sigma_D^2}\right) \tag{1}$$

where D_0 is the mean cluster diameter and σ_D is the diameter standard deviation. The distribution is asymmetric; it is steeper for small particles sizes (diameters) than for large diameters, and it is often used for describing the polydispersity of very small particles. The log-normal distribution holds not only for the diameters, but also for the volumes, with a volumetric standard deviation $\sigma_v = 3\sigma_D$. The average cluster volume can be expressed as [20]

$$\langle V \rangle = V_0 \exp\left(\frac{\sigma_v^2}{2}\right), \tag{2}$$

where $V_0 = \frac{\pi}{6} D_0^3$. The solid line in figure 3 is the log-normal function with $D_0 = 24$ Å and $\sigma_D = 0.17$. Thus, the average volume of the cluster is $\langle V \rangle = 8.243 \times 10^{-27}$ m^3, which corresponds to approximately 740 atoms per cluster.

Moreover, as seen from figure 2, the $Ni_{81}Fe_{19}$ particles are arranged periodically along the growth direction. This periodicity appears also in the low angle x-ray diffraction pattern (see figure 4, the upper curve), which displays first- and second-order Bragg peaks from the superlattices. The absence of higher order peaks in this reflectivity pattern implies a strong variation of the bilayer thickness, which is in agreement with the TEM observation. However, the nature of the imperfections is not apparent from the x-ray analysis.

The x-ray reflectivity curves obtained from the multilayers with different nominal thickness of the $Ni_{81}Fe_{19}$ layer are shown in figure 4. As seen from the figure, all films exhibit superlattice peaks, indicating a compositional modulation along the film growth direction. However, the high order peaks gradually decrease and the full widths at half-maxima (FWHM) of the first superlattice peaks tend to increase with decreasing nominal thickness of the $Ni_{81}Fe_{19}$ layers. This indicates an increment of the thickness variation of the layers. For the samples with nominal thickness of the $Ni_{81}Fe_{19}$ layer equal to 16 and 30 Å the intensities of the first-order Bragg peaks are comparable to the total internal reflection. The apparent decrease of the intensity below 1° originates from the footprint effect, since no footprint correction was performed.

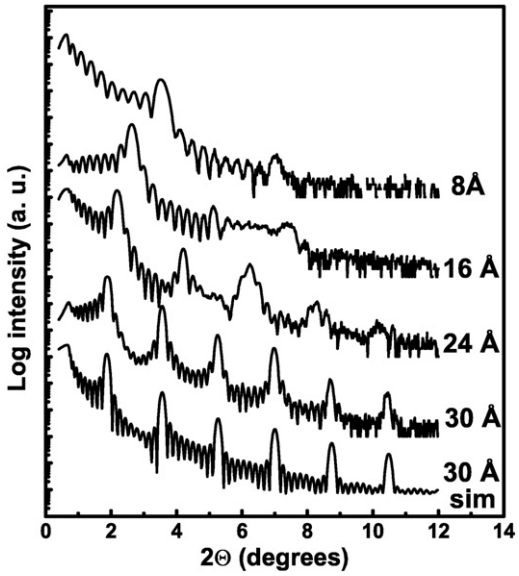

Figure 4. Low angle x-ray diffraction by $Al_2O_3/Ni_{81}Fe_{19}$ films with different thickness of the $Ni_{81}Fe_{19}$ layers. The four upper spectra are experimental whereas the lowermost curve is obtained by simulation for the $[Al_2O_3(18\ Å)/Ni_{81}Fe_{19}(30\ Å)]_{10}$ film. The introduced roughness parameters are 1 Å for $Ni_{81}Fe_{19}$ and 5 Å for Al_2O_3.

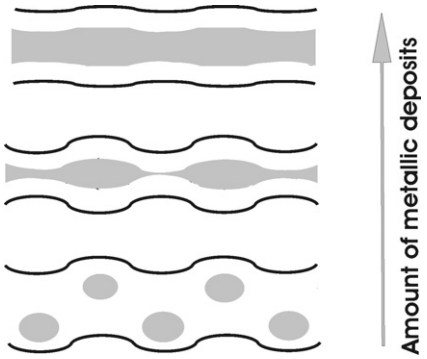

Figure 5. Schematic cross-sections of the $Ni_{81}Fe_{19}/Al_2O_3$ multilayered films. The grey colour indicates the metallic layer and the white colour is an isolating layer.

We performed a simulation of the reflectivity data by using GIXA [21]. The lowermost curve in figure 4 is a simulated curve for the film with 30 Å thick $Ni_{81}Fe_{19}$ layers. The best fit is achieved when the roughness parameters are about 1 and 5 Å for the $Ni_{81}Fe_{19}$ and Al_2O_3 layers, respectively. These values are, in principle, in agreement with the TEM studies (see figure 1), which reveal flat and well defined interfaces in that multilayer film. The simulation of the reflectivity diffractograms for the other samples, with non-planar interfaces, was performed in order to confirm the bilayer thickness, since due to the increased waviness of the layers the roughness parameter, as obtained from GIXA, does not take the actual interface geometry into account. The bilayer periods for the multilayers with $t_n > 8$ Å are found to agree with the nominal ones, which indicates that the layers grow continuously.

Finally, by combining the TEM and x-ray reflectometry studies we can analyse the evolution of the metal/Al_2O_3 interfaces with the thickness of metallic layers. The schematic illustration of that process is shown in figure 5. First, metallic atoms nucleate on the oxide surface in the islands' Volmer–Weber growth mode. The islands can have well defined spherical or elliptical shapes [22]. They are separated from each other by the next deposited oxide layer. If the amount of magnetic material deposited in one layer is increased, the islands grow until they reach the percolation threshold, implying extremely wavy metal–oxide interfaces. The

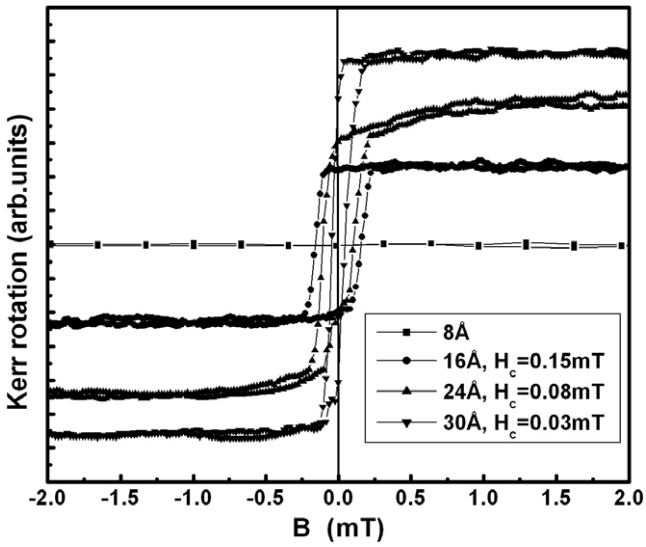

Figure 6. Room temperature magnetization curves for $Al_2O_3/Ni_{81}Fe_{19}$ multilayers. The nominal thicknesses of the metallic layers and corresponding the coercive fields are labelled on the graph. The horizontal line is a part of the magnetization curve for the film with 8 Å of $Ni_{81}Fe_{19}$, typical for a paramagnetic sample.

resulting interfaces have the morphology of alternating concave and convex surfaces. Since the concave surface has a smaller potential than the convex one, further deposition will lead to a preferential absorption of the atoms on the concave surface, in order to decrease the total energy of the system [23]. For very thick metallic layers, one obtains well defined flat interfaces. In the next subsection we show that the interface morphology strongly influences the magnetic properties of the $Al_2O_3/Ni_{81}Fe_{19}$ multilayers.

3.2. Magnetic properties

In figure 6 we present the MOKE hysteresis loops measured for all films at room temperature. The discontinuous sample (8 Å, $Ni_{81}Fe_{19}$ layers) shows a paramagnetic behaviour. This observation is consistent with the structural analysis. Small magnetic nanoclusters in an insulating matrix are expected to be superparamagnetic [5, 6]. The films with thicker $Ni_{81}Fe_{19}$ layers exhibit ferromagnetic behaviour, and the saturation magnetization gradually increases with increasing magnetic layer thickness. The coercive field of the ferromagnetic samples measured at room temperature is rather small, as expected for $Ni_{81}Fe_{19}$ alloys [17]. The coercivity decreases with increasing $Ni_{81}Fe_{19}$ layer thickness, consistent with increasing quality of the layered films. The coercive field is intimately linked to domain nucleation and to pinning of domain walls by structural defects [13].

In figure 7 field cooled (FC) and zero-field cooled (ZFC) magnetization curves are plotted as a function of temperature for the discontinuous (8 Å $Ni_{81}Fe_{19}$) and flat continuous (30 Å $Ni_{81}Fe_{19}$) multilayers. For ZFC magnetization, the samples were cooled down to 10 K in the absence of a magnetic field. Then, a field of 2 mT was applied and the magnetization was measured as the sample was heated up to 350 K. The FC magnetization was measured while cooling the sample to 10 K in the presence of 2 mT field.

As seen from the figure, ZFC–FC magnetization of the continuous multilayer film shows a ferromagnetic character, with an ordering temperature above room temperature. The ZFC magnetization curve for nanoparticles (figure 7(a)) presents a maximum at $T_{peak}(ZFC) = 30$ K and irreversibility between ZFC and FC magnetization below that maximum. This indicates that the particles undergo a superparamagnetic relaxation process and are expected to be single-

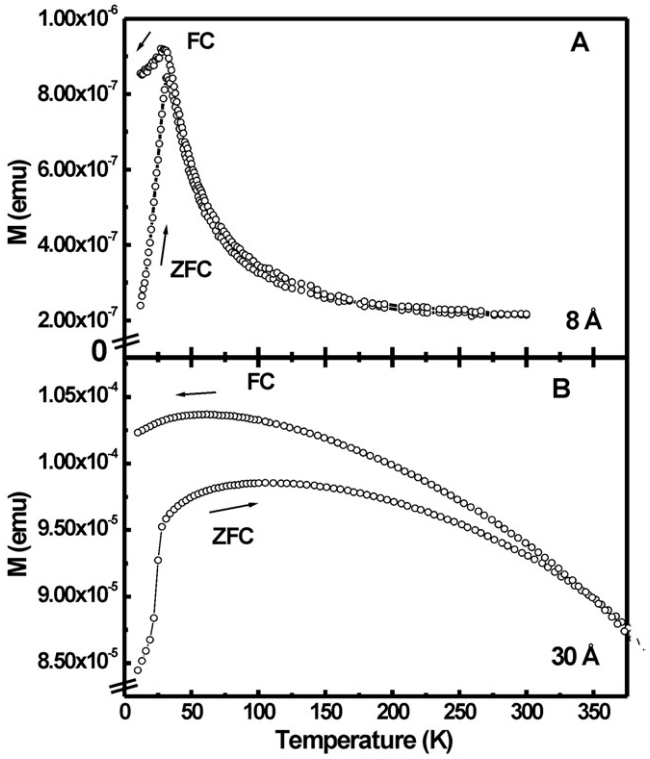

Figure 7. Zero-field cooled and field cooled magnetization curves for an applied field of 2 mT, as a function of temperature for the nanoparticles (A) and multilayers (B). The labels on the graphs correspond to the nominal thickness of a $Ni_{81}Fe_{19}$ layer.

domain particles [24] whose anisotropy energy barrier is of the same magnitude as the thermal energy [25]. Therefore, using the data obtained from structural analysis and from the FC–ZFC magnetization, we can estimate the anisotropy strength of the $Ni_{81}Fe_{19}$ nanoparticles. As is known from the literature [20], the anisotropy constant K for superparamagnetic particles of mean volume $\langle V \rangle$ can be estimated from the following equation:

$$k_B \langle T_b \rangle = \frac{K \langle V \rangle}{\ln(\frac{\tau_m}{\tau_0})}. \tag{3}$$

where $\tau_m \approx 100$ s is the timescale characteristic of the measurement technique and τ_0 is a microscopic relaxation time, which is of the order of 10^{-10} s for ferromagnetic and ferrimagnetic materials. $\langle T_b \rangle$ is a mean blocking temperature. The blocking temperature is defined as the temperature for which the relaxation time of the particles equals τ_m. However, since the particles have a size distribution, one may consider the smaller particles, with the relaxation time smaller than τ_m, to behave as paramagnetic objects, whereas the larger ones with $\tau > \tau_m$ are blocked. It is common to refer to a mean blocking temperature for the assembly of small particles. $\langle T_b \rangle$ can be roughly estimated as $T_{peak}(\mathrm{ZFC})$. However, as shown by Sappey *et al* [19], the ZFC peak position depends on the volumetric standard deviation σ_v of the particle size distribution, and shifts extremely rapidly towards higher temperatures when σ_v is increased. Therefore, the width of the distribution has to be taken into account. The mean blocking temperature can be determined from the ratio $\alpha = T_{peak}(\mathrm{ZFC})/\langle T_b \rangle$, where α depends on σ_v [19] and is equal to 2 for $\sigma_v = 0.5$. This value of σ_v was obtained from the structural analysis (see equation (2)). Besides that, the dipolar interactions between the particles have to be taken into account, since equation (3) is only valid for non-interacting nanoparticles. As observed in our previous investigation on films with similar distributions of particles, but with

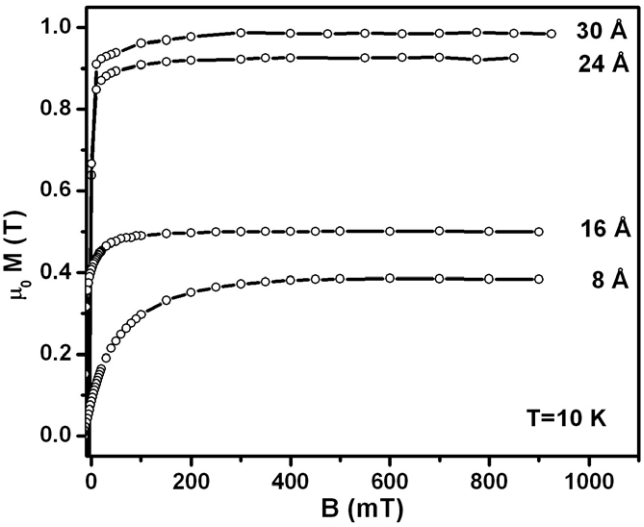

Figure 8. Normalized magnetization versus applied field for $Al_2O_3/Ni_{81}Fe_{19}$ multilayers. The labels correspond to the nominal thickness of a metallic layer. The diamagnetic contribution, mainly due to the Si substrate, has been subtracted.

different distances between them [24], the weakly interacting particles have ZFC maximum temperatures at about 17 K. This temperature can be used as T_{peak}(ZFC) in the present case. Thus, the mean blocking temperature is found to be about 8.5 K and the anisotropy constant for the nanoparticles, determined from equation (3), is equal to $|K| \approx 3.9 \times 10^5$ J m^{-3}. This anisotropy constant is an effective value which includes surface, magnetocrystalline and shape contributions, and it appears to be two orders of magnitude higher than the anisotropy constant for bulk $Ni_{81}Fe_{19}$ ($|K| \approx 1.5 \times 10^3$ J m^{-3} [17]). This result is consistent with the large fraction of surface atoms in the metallic particles.

The changes in the hysteresis loops with increasing $Ni_{81}Fe_{19}$ layer thickness are seen in figure 8, where the magnetization versus applied magnetic field at 10 K is plotted for the four samples. As seen in the figure, the samples exhibit magnetic anisotropy which can be ascribed to the waviness of the magnetic layer. This anisotropy can be caused by magnetization fluctuation from its easy direction in the interface region when the waviness of the interfaces reaches its maximum.

The normalized saturation magnetization and, consequently, the value of the magnetic moment per metallic atom increase when the $Ni_{81}Fe_{19}$ layer becomes thicker and the magnetic moment for the thickest film approaches the bulk value of 1.0 μ_B/atom [17]. The magnetic moment decrement may be explained by the magnetic inhomogeneity across the $Ni_{81}Fe_{19}$ layer. Indeed, thin antiferromagnetic oxide layers have been proved to exist at the Ni/alumina [16] and Fe/alumina [15] interfaces, since the chemical bonding between metal and oxygen is a part of the adhesion mechanism at metal–ceramic interfaces [14]. The extension of the region with reduced magnetic moments can be estimated for the two extreme cases: flat, well defined layers and spherical clusters. For simplicity we assume that the magnetic moment at the interfaces is equal to zero. Hence, the fraction of atoms which belong to the interfaces, f_{int}, can be expressed as

$$f_{\text{int}} = \frac{m_B - m}{m_B} \tag{4}$$

where m_B is the magnetic moment of $Ni_{81}Fe_{19}$ in the bulk [17], m is the magnetic moment per atom in the film. In cases of continuous films, one can obtain the thickness of the interface layer from the following argumentation. The volume of nonmagnetic atoms at the interfaces

Table 1. Structural and magnetic parameters of $Al_2O_3/Ni_{81}Fe_{19}$ multilayers.

t_n of $Ni_{81}Fe_{19}$ layer	m (μ_B/atom)	f_{int}	Δ (Å)
8	0.366	0.64	3.8
30	0.938	0.07	1

V_{int} is given by

$$V_{int} = A t_n f_{int} \tag{5}$$

where A is the film area, t_n is the nominal thickness of the film. On the other hand, V_{int} can also be expressed as

$$V_{int} = A_{int} 2\Delta \tag{6}$$

where A_{int} is the area occupied by nonmagnetic atoms and Δ is the interface layer thickness. By comparing equations (5) and (6) one can obtain

$$\frac{A_{int}}{A} = \frac{t_n f_{int}}{2\Delta}. \tag{7}$$

We consider the interfaces in the 30 Å film to be flat and, hence, the ratio $\frac{Aint}{A}$ is equal to 1 in that case. Thus, from equation (7) we can determine the thickness of the nonmagnetic layer to be about 1 Å at each interface.

In cases of spherical clusters, the fraction of nonmagnetic atoms is a ratio of interface atom volume to the total volume of $Ni_{81}Fe_{19}$ and can be expressed as

$$f_{int} = 1 - \frac{\int_{2\Delta}^{\infty} p(D)(D-2\Delta)^3 \,\mathrm{d}D}{\int_0^{\infty} p(D) D^3 \,\mathrm{d}D} \tag{8}$$

where $p(D)$ is a log-normal distribution function for the clusters (equation (1)). The lower integration limit is 2Δ since the clusters with $D \leqslant 2\Delta$ are completely nonmagnetic. The integration in equation (8) was done numerically and Δ was determined to be about 3.8 Å. The summary of results is presented in table 1.

As seen in the table, the thickness of nonmagnetic layers in the continuous multilayer film is considerably smaller than that in the discontinuous sample. Even if the uncertainty in the surface area determination were as high as 30%, the difference between Δ for nanoclustered and continuous multilayers would still be significant. This may indicate that the approximation of a spherical shape and a smooth surface for the particles is not accurate enough. The particles may have elongated shapes with rough, stepped interfaces. These factors imply an excess in the particles surface area, thus indicating that the surface area may be underestimated within the present model.

4. Conclusions

In conclusion, $Ni_{81}Fe_{19}/Al_2O_3$ multilayers were produced by a sequential magnetron sputter deposition. It was shown that the structure can be controlled from nanoparticles to flat continuous layers, merely by varying the thickness of the metallic layer from 8 to 30 Å. Considering the growth mechanism of metal–ceramic heterostructures, and applying structural analysis, we argue that the waviness of the $Ni_{81}Fe_{19}$/alumina interfaces scales with the $Ni_{81}Fe_{19}$ layer thickness. Apparently, the interface morphology influences the magnetic properties of the multilayers studied. The sample with discontinuous metallic particles is found to be

superparamagnetic while the samples with continuous metallic layers show ferromagnetic behaviour.

A large fraction of surface atoms in metallic particles leads to a significant increment of the anisotropy constant for the discontinuous film, as compared to that for bulk samples. Furthermore, the magnetic anisotropy in the continuous films can be ascribed to the waviness of the magnetic layers. The reduction of the magnetic moment per metallic atom in the multilayers can be caused by the presence of thin antiferromagnetic oxide layers at the interfaces. Using the assumption of zero roughness for the continuous layers and a smooth spherical shape for the nanoparticles, we calculated the thickness of the nonmagnetic layers for the films with 30 and 8 Å thick $Ni_{81}Fe_{19}$ layers. It was found that the thickness of a nonmagnetic layer (3.8 Å) in the sample with metallic particles is noticeably higher than that (1 Å) in the sample with continuous metallic layers. This indicates that the particles may have rough stepped surfaces, which has not been considered in the present model.

Acknowledgments

ILS would like to acknowledge fruitful discussions with P Korzhavyi and R Bručas. This work has been supported by the Swedish Foundation for Strategic Research (SSF) through the FRAM project and by the Swedish Research Council (VR).

References

[1] Julliere X 1975 *Phys. Lett.* A **54** 225
[2] Moodera J S and Mathon G 1999 *J. Magn. Magn. Mater.* **200** 248
[3] Sun J Z, Roche K P and Parkin S S P 2000 Materials science of novel oxide-based electronics. Symposium *Mater. Res. Soc. Symp. Proc.* **623** 51
[4] Zhu W, Hirschmugl C J, Laine A D, Sinkovic B and Parkin S S P 2001 *Appl. Phys. Lett.* **78** 3103
[5] Oleinik I I, Tsymbal E Yu and Pettifor D G 2000 *Phys. Rev.* B **62** 3952 and references therein
[6] Bowen M, Cros V, Petroff F, Fert A, Martinez Boubeta C, Costa-Krämer J L, Anguita J V, Cebollada A, Briones F, de Teresa J M, Morellon L, Ibarra M R, Güell F, Peiro F and Cornet A 2001 *Appl. Phys. Lett.* **79** 1655
[7] Chapman B 1980 *Glow Discharge Processes* (New York: Wiley)
[8] Schad R, Mayen K, McCord J, Allen D, Yang D, Tondra M and Wang D 2001 *J. Appl. Phys.* **89** 6659
[9] Teixeira S R, Boff M A S, Flores W H, Schmidt J E, Alves M C M and Tolentino H C N 2001 *J. Magn. Magn. Mater.* **233** 96
[10] Kumar D, Narayan J, Nath T K, Sharma A K, Kvit A V and Jin C 2001 *Solid State Commun.* **119** 63
[11] Kumar D, Narayan J, Kvit A V, Sharma A K and Sankar J 2001 *J. Magn. Magn. Mater.* **232** 161
[12] Lym H-S, Jeon D-M, Baek H-K, Yoon S-Y, Lee D-H, Yoon D-H and Suh S-J 2001 *Japan. J. Appl. Phys.* **40** 6360
[13] Cai J-W, Okamoto S, Kitakami O and Shimada Y 2001 *Phys. Rev.* B **63** 104418
[14] Johnson K H and Pepper S V 1982 *J. Appl. Phys.* **53** 6634
[15] Arranz A, Pérez-Dieste V and Palacio C 2002 *Surf. Sci.* **521** 77
[16] Ealet B, Gillet E, Nehasil V and Møller P J 1994 *Surf. Sci.* **318** 151
[17] Bozorth Richard M 1956 *Ferromagnetism* (Princeton, NJ: Van Nostrand-Reinhold) chapter 5
[18] Kaiser R and Miskolczy G 1970 *J. Appl. Phys.* **41** 1064
[19] Sappey R, Vincent E, Hadacek N, Chaput F, Boilot J P and Zins D 1997 *Phys. Rev.* B **56** 14551
[20] Ngo A T, Bonville P and Pileni M P 1999 *Eur. Phys. J.* B **9** 583
[21] de Boer D K G and van den Hoogenhof W W 1991 *Spectrochim. Acta* B **46** 1323
[22] Maurice J-L, Briático J, Carrey J, Petroff F, Schelp L F and Vaurés A 1999 *Phil. Mag.* A **79** 2921
[23] Cao G 2004 *Nanostructures and Nanomaterials—Synthesis, Properties and Applications* (London: Imperial College Press) chapter 2
[24] Stanciu V, Soroka I L, Lu J, Hjörvarsson B and Nordblad P 2005 *J. Magn. Magn. Mater.* **286** 446
[25] Bean C P and Livingston J D 1959 *J. Appl. Phys.* **30** 120S